Electronic Supplementary Information for

Intrinsic carbon defect-engineered carbonized wood membrane electrodes for superior supercapacitors

Zhengguo Zhang,[a,b] Jinyu Ma,[a,b] Fang Wang,[a,b] Yaming Kang*[c] and Shixiong Min*[a,b,d]

[a] *School of Chemistry and Chemical Engineering, North Minzu University, Yinchuan, 750021, P. R. China.*

[b] *Ningxia Key Laboratory of Solar Chemical Conversion Technology, North Minzu University, Yinchuan, 750021, P. R. China.*

[c] *School of Electrical and Mechanical Engineering, North Minzu University, Yinchuan, 750021, P. R. China.*

[d] *Analysis and Testing Center of Ningxia Hui Autonomous Region, North Minzu University, Yinchuan, 750021, P. R. China.*

*Corresponding author: scu.kym@foxmail.com; sxmin@nun.edu.cn

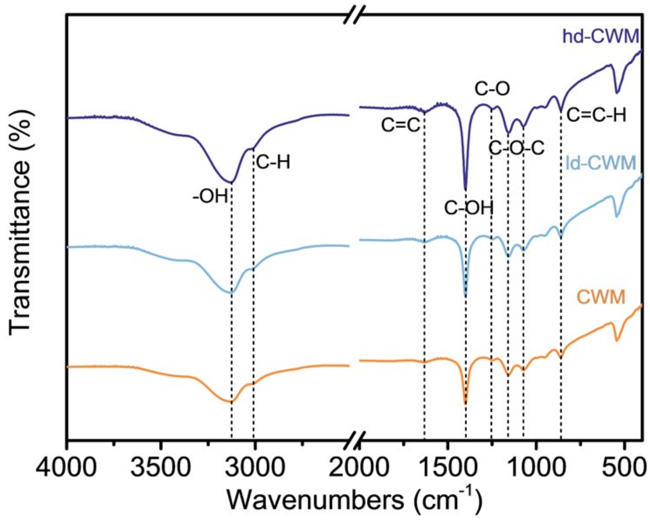

Fig. S1 FTIR spectra of hd-CWM, ld-CWM, and CWM electrodes.

Table S1 Textural properties of CWM, ld-CWM, and hd-CWM obtained at different etching temperatures.

Electrode	S_{BET} (m^2 g^{-1})^a	Pore volume (cm^3 g^{-1})^b	Pore size (nm)^c
CWM	75.8	0.04	2.18
ld-CWM	527.9	0.31	2.34
hd-CWM (550 °C)	242.5	0.14	2.34
hd-CWM (650 °C)	699.1	0.37	2.13
hd-CWM (750 °C)	913.8	0.53	2.30
hd-CWM (850 °C)	739.9	0.41	2.20

^{a} BET surface area (S_{BET}) is calculated from the linear part of the BET plot.

^{b} Single point total pore volume of the pores at P/P_0=0.99.

^{c} Adsorption average pore width (4 V A^{-1} by BET).

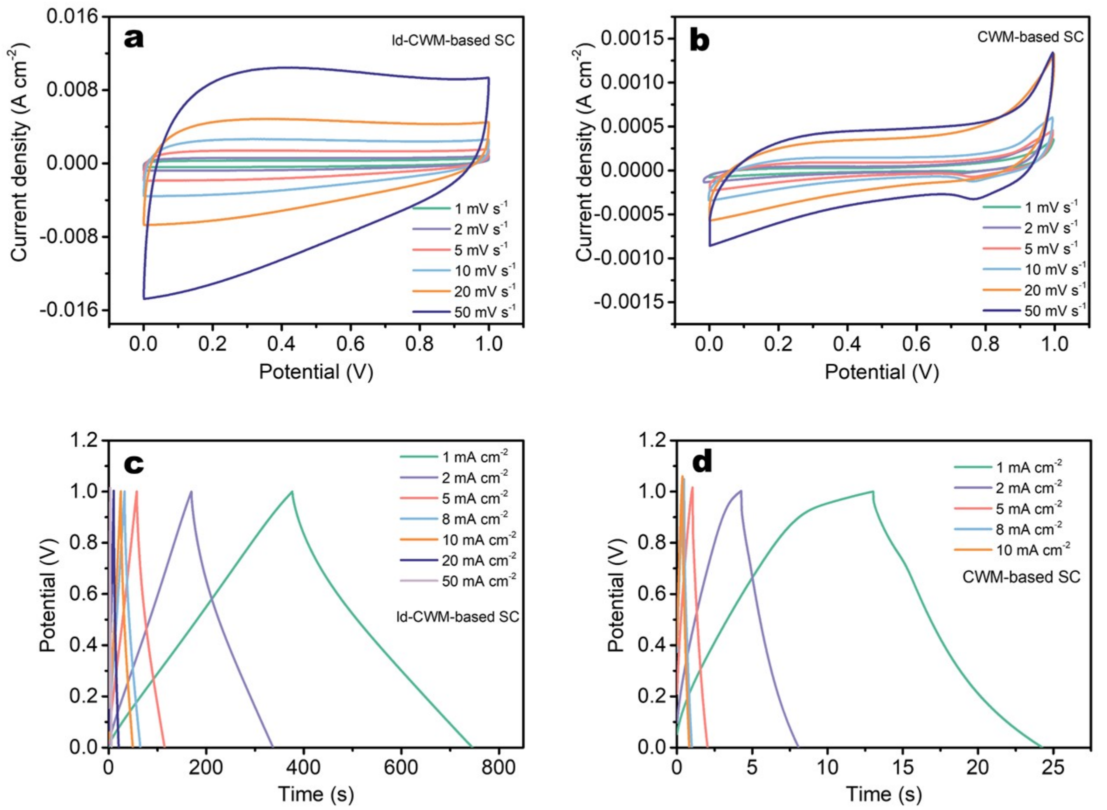

Fig. S2 CV curves of (a) ld-CWM-based SC and (b) CWM-based SC. GCD curves of (c) ld-CWM-based SC and (d) CWM-based SC.

Table S2 Series resistance (R_s) and electron transfer resistance (R_{ct}) of the hd-CWM-, ld-CWM-, and CWM-based SCs

SC	R_s (Ω)	R_{ct} (Ω)
hd-CWM-based SC	0.47	0.15
ld-CWM-based SC	0.97	0.16
CWM-based SC	0.68	0.62

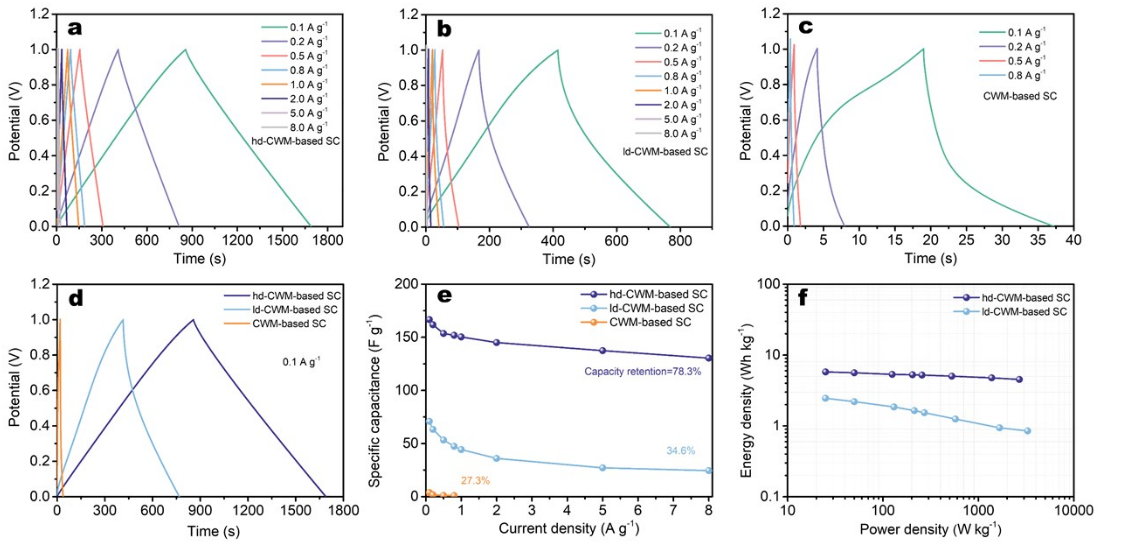

Fig. S3 GCD curves of (a) hd-CWM-, (b) ld-CWM-, and (c) CWM-based SCs at different current densities. (d) GCD curves at 0.1 A g^{-1} and (e) the corresponding C_m values of the hd-CWM-, ld-CWM-, and CWM-based SCs. (f) Ragone plots (mass energy density vs. mass power density) of hd-CWM-, and ld-CWM-based SCs.

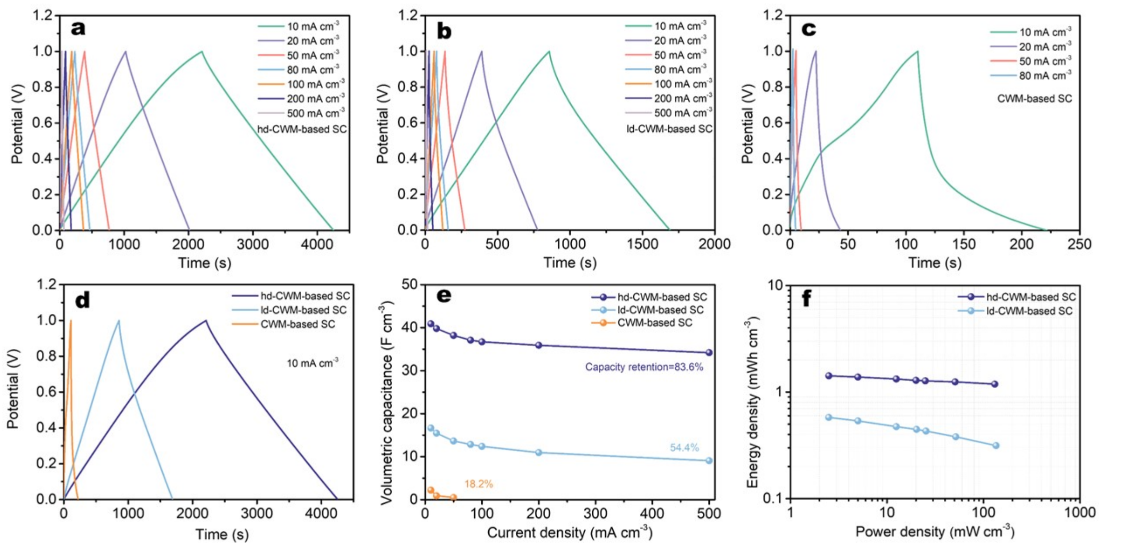

Fig. S4 GCD curves of (a) hd-CWM-, (b) ld-CWM-, and (c) CWM-based SCs at different current densities. (d) GCD curves at 10 mA cm^{-3} and (e) the corresponding C_v values of the hd-CWM-, ld-CWM-, and CWM-based SCs. (f) Ragone plots (volumetric energy density vs. volumetric power density) of hd-CWM- and ld-CWM-based SCs.

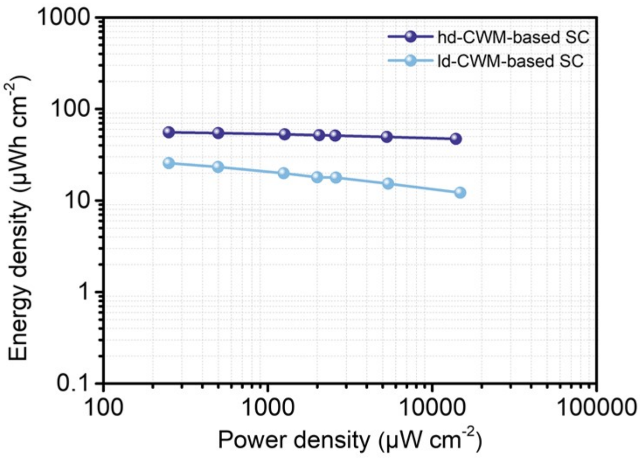

Fig. S5 Ragone plots (areal energy density vs. areal power density) of hd-CWM- and ld-CWM-based SCs.

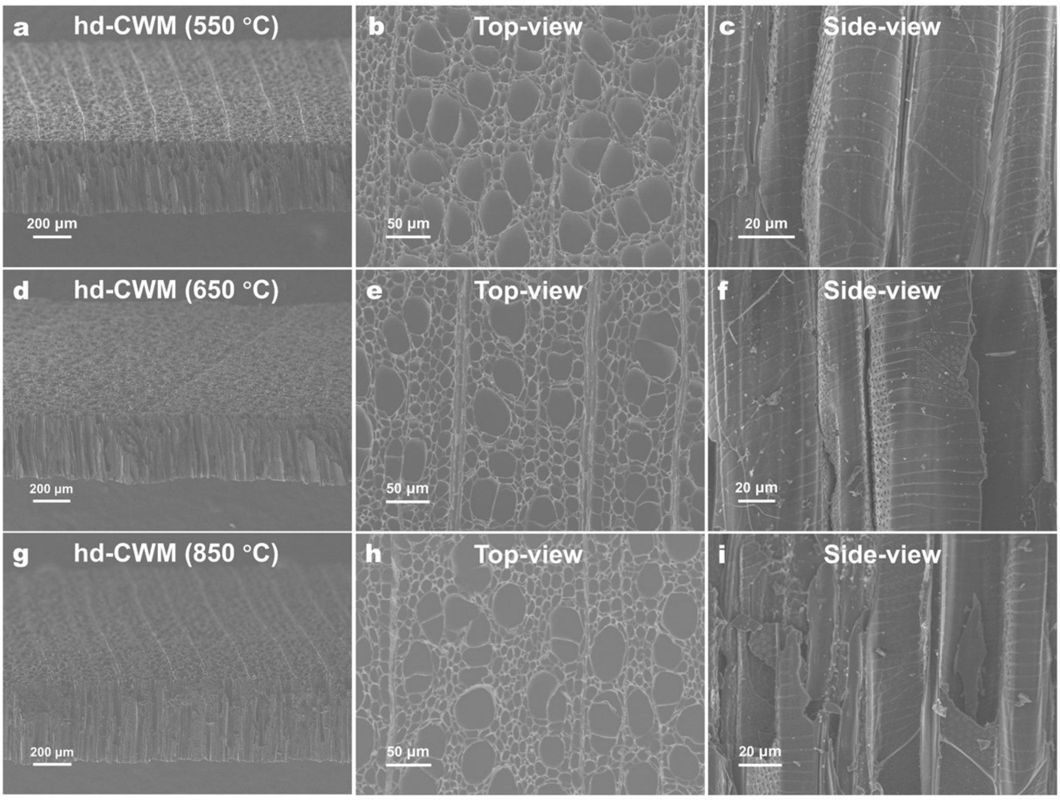

Fig. S6 SEM images of hd-CWM electrodes prepared at different etching temperatures of (a-c) 550 ^{o}C, (d-f) 650 ^{o}C, and (g-i) 850 ^{o}C.

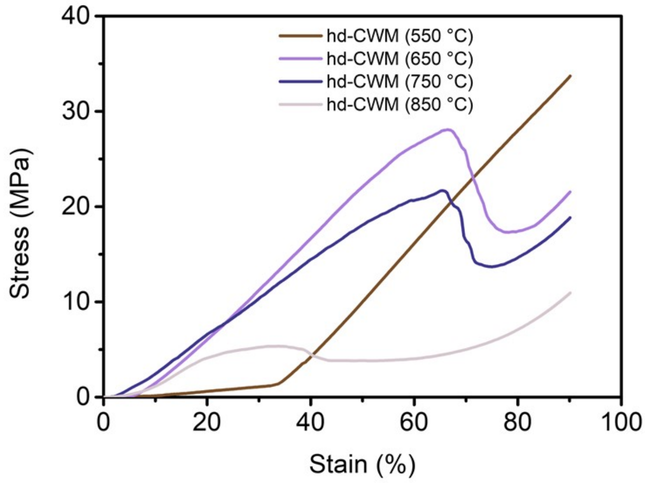

Fig. S7 Stress-strain curves of hd-CWM electrodes prepared at different etching temperatures.

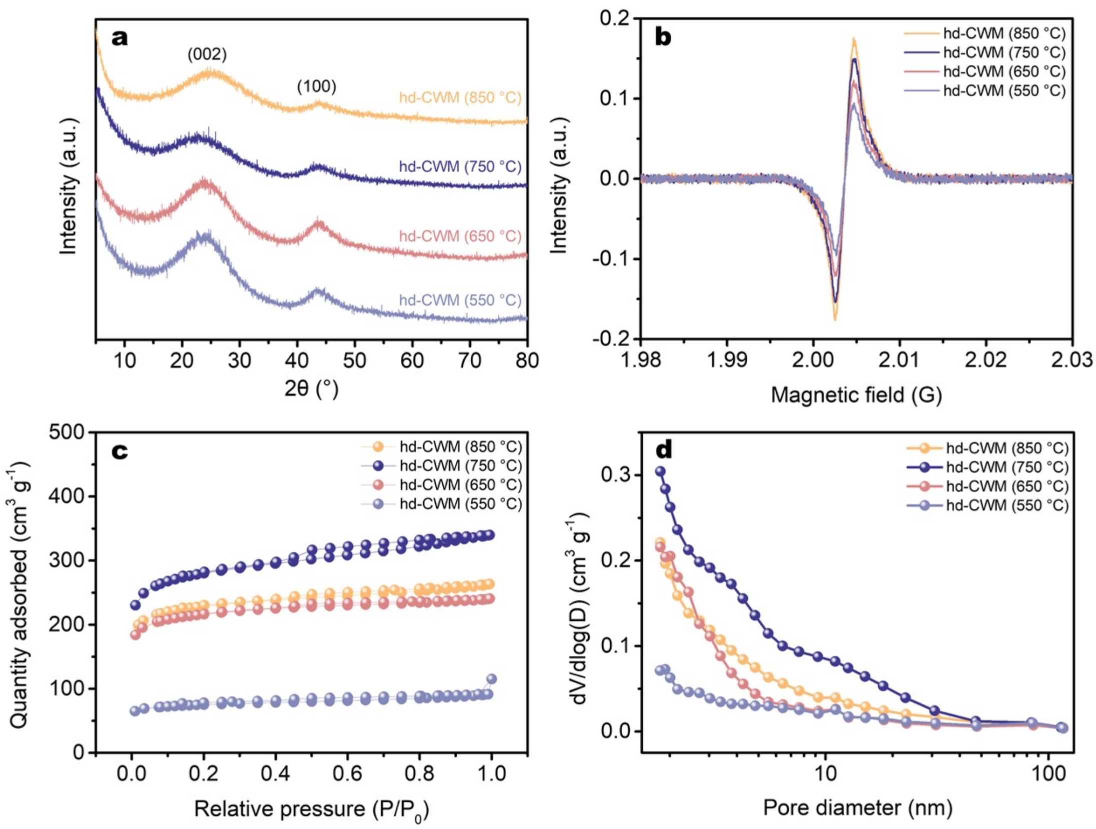

Fig. S8 (a) XRD spectra, (b) EPR spectra, (c) N_2 adsorption-desorption profiles and the corresponding (d) pore size distribution curves of hd-CWM electrodes prepared at different etching temperatures.

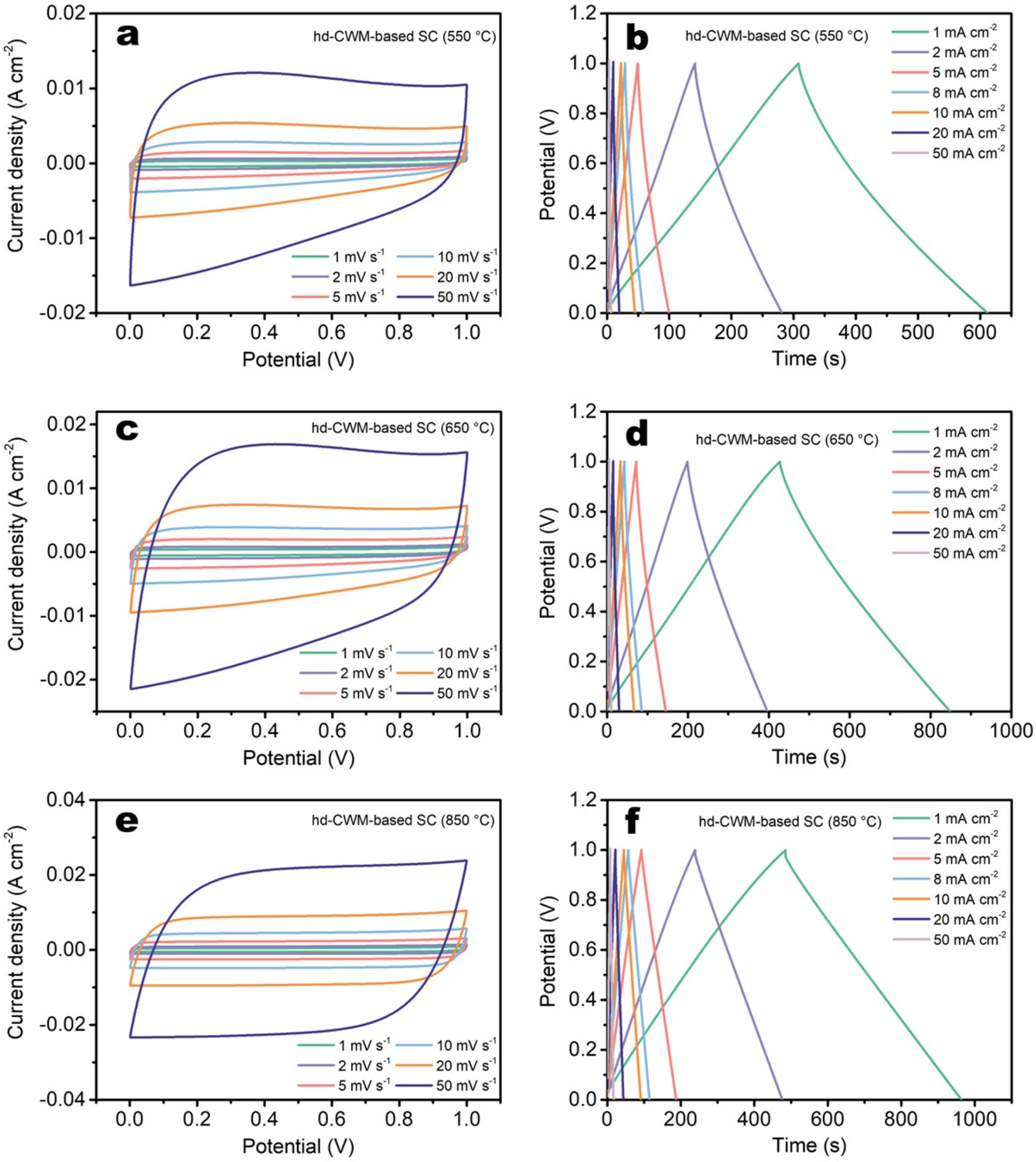

Fig. S9 CV and GCD curves of the SCs assembled with hd-CWM electrodes prepared at different etching temperatures.

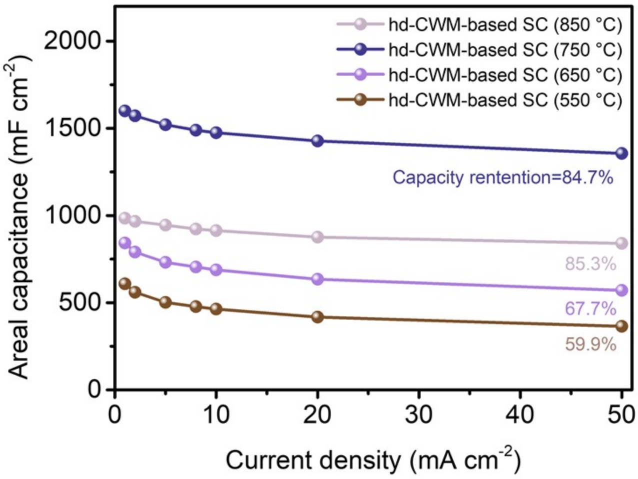

Fig. S10 C_a values of the SCs assembled with hd-CWM electrodes prepared at different etching temperatures.

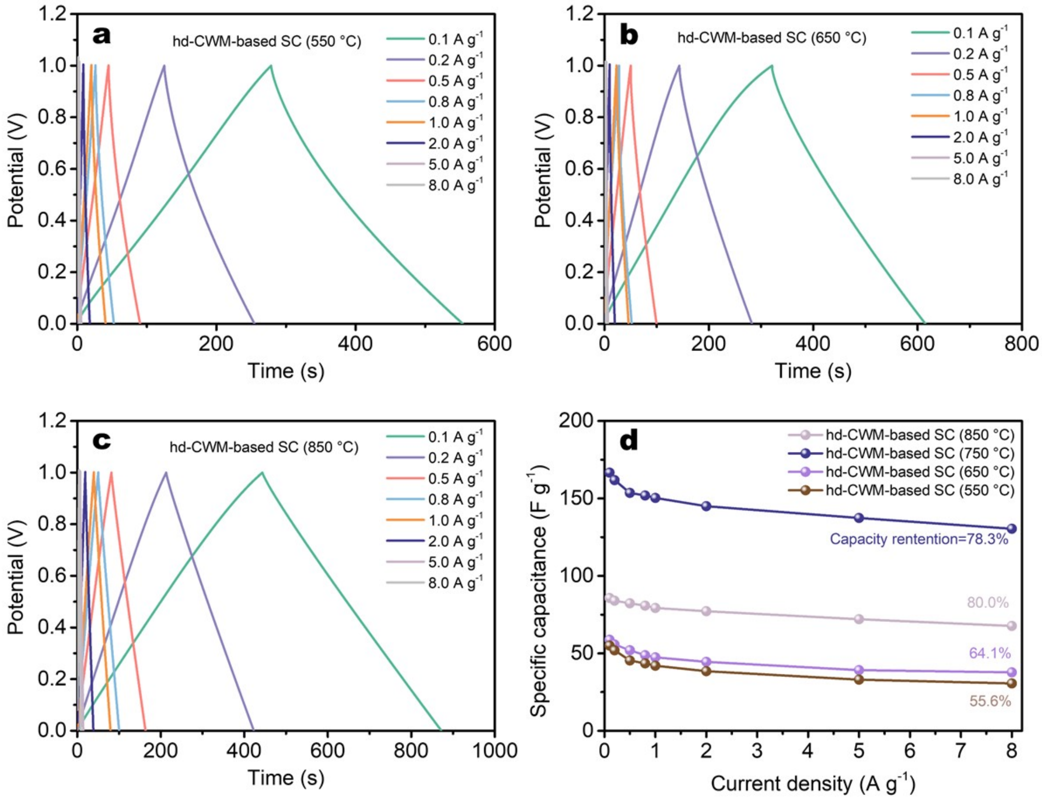

Fig. S11 GCD curves of the SCs assembled with hd-CWM electrodes prepared at different etching temperatures of (a) 550, (b) 650, and (c) 850 °C and the corresponding (d) C_m values at difference current densities.

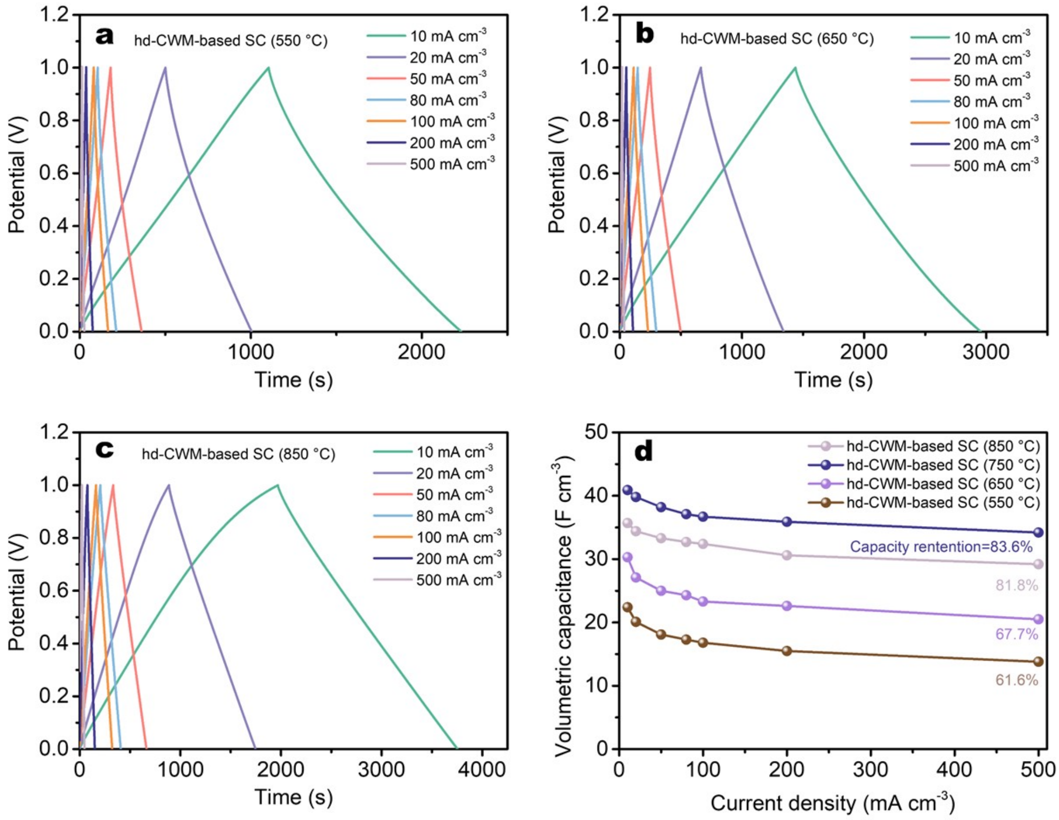

Fig. S12 GCD curves of the SCs assembled with hd-CWM electrodes prepared at different etching temperatures of (a) 550, (b) 650, and (c) 850 ^{o}C and the corresponding (d) C_v values at difference current densities.

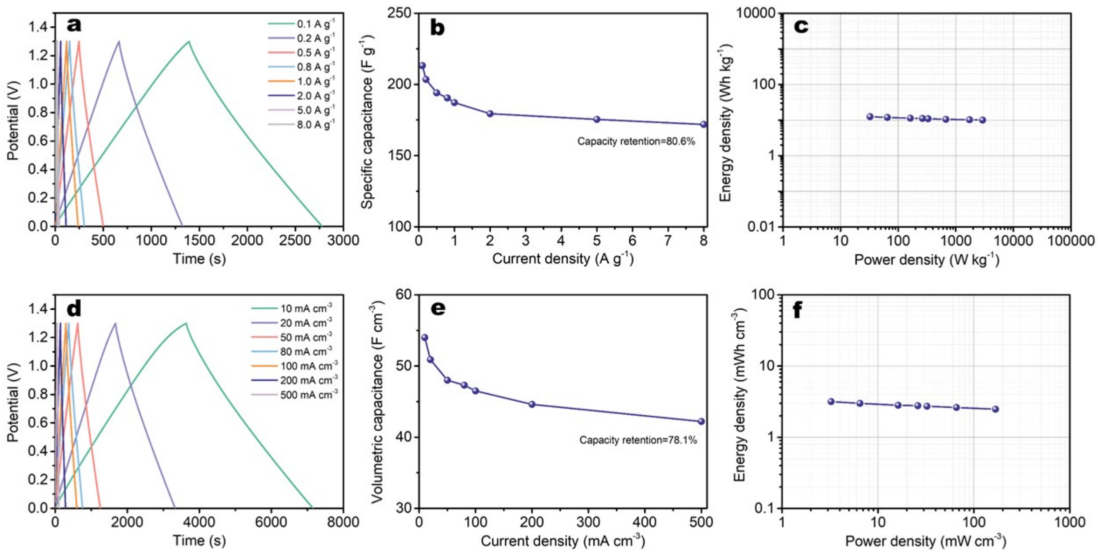

Fig. S13 (a) GCD curves, (b) C_m values of hd-CWM-based SC at different current densities, and (c) the corresponding Ragone plot. (d) GCD curves, (e) C_v values of hd-

CWM-based SC at different current densities, and (f) the corresponding Ragone plot.

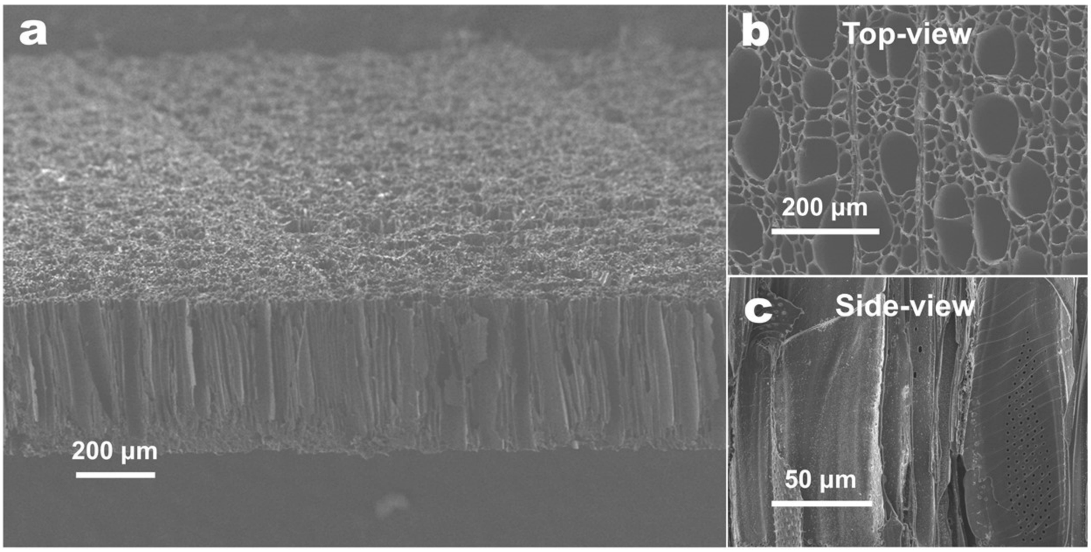

Fig. S14 (a-c) SEM images of hd-CWM electrode after cycling stability test in the potential window of 0-1.3 V at a current density of 10 mA cm^{-2}.

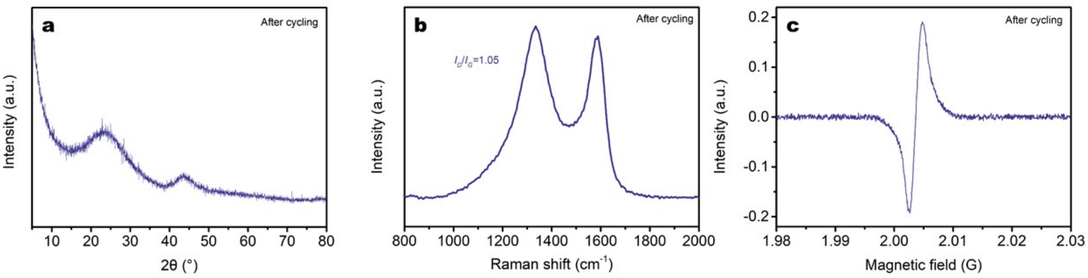

Fig. S15 (a) XRD spectrum, (b) Raman spectrum, and (c) EPR spectrum of hd-CWM electrode after cycling stability test in the potential window of 0-1.3 V at a current density of 10 mA cm^{-2}.

Table S3 Comparison of electrochemical performance of the hd-CWM-based SC with reported carbon-based SCs.

Electrode	Electrolyte	C_a or C_m	Energy Density	Cycling stability	Ref.
PCN/CW	6.0 M KOH	5547 mF cm^{-2} (5 mA cm^{-2})	0.26 mWh cm^{-2} (1.19 mW cm^{-2})	97.4% (10000 cycles)	1
WTCS	6.0 M KOH	286 F g^{-1} (1 A g^{-1})	9.9 Wh kg^{-1} (250 W kg^{-1})	95.0% (5000 cycles)	
FA-OC2	6.0 M KOH	5037.5 mF cm^{-2} (2 mA cm^{-2})	0.65 mWh cm^{-2} (58.0 mW cm^{-2})	86.3% (20000 cycles)	3
CWM@PANI	1.0 M H_2SO_4	639.5 F g^{-1} (0.5 A g^{-1})	43.11 Wh kg^{-1} (350 W kg^{-1})	88.5% (5000 cycles)	4
C-RS-BL	6.0 M KOH	4100 mF cm^{-2} (1 mA cm^{-2})	0.82 mWh cm^{-2} (0.6 mW cm^{-2})	85.7% (10000 cycles)	
HBC-2M	1.0 M Na_2SO_4	2368.0 mF cm^{-2} (1 mA cm^{-2})	87 μWh cm^{-2} (470 μW cm^{-2})	87.5% (2000 cycles)	
CC	6.0 M KOH	99 F g^{-1} (0.1 A g^{-1})	3.44 Wh kg^{-1} (25 W kg^{-1})	104% (20000 cycles)	
CNTs/NF	6.0 M KOH	319.1 mF cm^{-2} (1 mA cm^{-2})	n. p	96.4% (10000 cycles)	
CGCM@GNS&CNT	1.5 M Na_2SO_4	441 mF cm^{-2} (1 mA cm^{-2})	31 μWh cm^{-2} (800 μW cm^{-2})	102.5 % (2000 cycles)	
BCPC-3	6.0 M KOH	330 F g^{-1} (0.5 A g^{-1})	6.1 Wh kg^{-1} (25 W kg^{-1})	90.0% (5000 cycles)	
hd-CWM	6.0 M KOH	1599.8 mF cm^{-2}/166.6 F g^{-1} (1 mA cm^{-2}/0.1 A g^{-1})	55.5 μWh cm^{-2}/5.8 Wh kg^{-1} (250 μW cm^{-2}/25 W kg^{-1})	116.3% (10000 cycles)	T w

n. p: Not applicable.

Supplementary references

1 Q. Wang, L. Fan, Z. Li, C. Li, C. Dong, C. Wang, M. Guo, X. Zhang, X. Zhou, L. Sheng, L. Jiang, Wood and PAN-derived hierarchically porous low-tortuosity carbon electrodes for high-areal-performance supercapacitors, *J. Energy Storage*, 2024, **78**, 110014.

2 J. Wu, M. W. Xia, X. Zhang, Y. Q. Chen, F. Sun, X. H. Wang, H. P. Yang and H. P. Chen, Hierarchical porous carbon derived from wood tar using crab as the template: Performance on supercapacitor, *J. Power Sources*, 2020, **455**, 227982.

3 B. Yan, J. J. Zheng, L. Feng, C. Du, S. J. Jian, W. S. Yang, Y. M. A. Wu, S. H. Jiang, S. J. He and W. Chen, Wood-derived biochar as thick electrodes for high-rate performance supercapacitors, *Biochar*, 2022, **4**, 50.

4 M. X. Cui, F. Wang, Z. G. Zhang and S. X. Min, Polyaniline-filled carbonized wood membrane as an advanced self-supported electrode for superior pseudocapacitive energy storage, *Electrochim. Acta*, 2020, **359**, 136961.

5 Y. Tang, X. Lin, J. Liao, J. Tan, Y. He, X. Cui, All-rice straw-derived self-supporting biochar to construct an ecological supercapacitor, *Ind. Crops Prod.*, 2025, **231**, 121220.

6 J. Zhang, L. Lin, T. Jiang, J. Cao, J. Zhang, J. Qin, H. Liang, White-rot fungal pretreatment for high-performance bamboo-derived carbon-based supercapacitor electrodes, *Molecules*, 2025, **30**, 3430.

7 Y. Zhang, Y. Cai, T. Li, M. Wang, X. Chen, and Y. Xu, Synthesis and electrochemical performance of biomass-derived porous carbon materials for supercapacitors, *J. Mater. Sci.: Mater. Electron.*, 2024, **35**, 116.

8 S.-H. Kao, K. S. Anuratha, S.-Y. Wei, J.-Y. Lin, C.-K. Hsieh, Facile and rapid electrochemical conversion of Ni into $Ni(OH)_2$ thin film as the catalyst for direct growth of carbon nanotubes on Ni foam for supercapacitors, *Nanomater.*, 2022, **12**, 3867.

9 W. W. He, P. G. Ren, Z. Dai, X. Hou, F. Ren and Y. L. Jin, Hierarchical porous carbon composite constructed with 1-D CNT and 2-D GNS anchored on 3-D carbon

skeleton from spent coffee grounds for supercapacitor, *Appl. Surf. Sci.*, 2021, **558**, 149899.

10 J.-k. Ou, H.-w. Zhang, Y. Lei, K.-y. Li, B. Li, H.-x. Deng, H. Wang and L. Zou, Buckwheat core derived nitrogen-and oxygen-rich controlled porous carbon for high-performance supercapacitors, *J. Cent. South Univ.*, 2023, **30**, 419-433.